Poiseuille flow of Lennard-Jones fluids in narrow slit pores

Karl P. Travis[a] and Keith E. Gubbins
*Department of Chemical Engineering, Riddick Labs, North Carolina State University,
Raleigh, North Carolina 27695-7905*

We present results from nonequilibrium molecular dynamics (NEMD) simulations of simple fluids undergoing planar Poiseuille flow in a slit pore only a few molecular diameters in width. The calculations reported in this publication build on previous results by including the effects of attractive forces and studying the flow at narrower pore widths. Our aims are: (1) to examine the role of attractive forces in determining hydrodynamic properties, (2) to provide clearer evidence for the existence of a non-Markovian generalization of Newtons law, (3) to examine the slip-stick boundary conditions in more detail by using a high spatial resolution of the streaming velocity profiles, (4) to investigate the significance of the recently proposed cross-coupling coefficient on the temperature profiles. The presence of attractive interactions gives rise to interesting packing effects, but otherwise, does not significantly alter the spatial dependence of hydrodynamic quantities. We find the strongest evidence to date that Newton's Law breaks down for very narrow pores; the shear viscosity exhibits singularities. We suggest a method to test the validity of the non-Markovian generalization of Newton's Law. No-slip boundary conditions are found to apply, even at these microscopic length scales, provided one takes into account the finite size of the wall atoms. The effects of any strain rate induced coupling to the heat flow are found to be insignificant. © *2000 American Institute of Physics.* [S0021-9606(00)50304-3]

I. INTRODUCTION

Classical Navier–Stokes (NS) hydrodynamic theory, applied to structureless fluids, predicts that in the case of planar Poiseuille flow, the streaming velocity of the fluid should depend quadratically on the coordinate normal to the confining boundaries. The NS equations assume that the transport coefficients are independent of position and time, and that the state variables of temperature and density do not vary appreciably, on length and time scales comparable to the molecular mean free path and molecular relaxation time. Computer simulation studies of confined fluids (see, for example, Refs. 1–10) show that the density in the direction of confinement can vary appreciably, especially close to the walls. In these cases it is therefore expected that the Navier–Stokes equations should fail. However, despite this, it is a remarkable fact that approximately quadratic velocity profiles are obtained in planar Poiseuille flow simulations of simple fluids confined to channels only 10 molecular diameters in width.[9] Deviations from classical predictions are present, but they appear to be weak; for example, the shear stress exhibits weak oscillations about the classical linear profile. At pore widths less than about 10 molecular diameter, the velocity profiles are no longer quadratic.[9,11]

In this publication we present nonequilibrium molecular dynamics (NEMD) simulation results for simple fluids undergoing planar Poiseuille flow, building on previous results by including the effects of attractive forces and studying the

flow at narrower pore widths. Our aims are (1) to examine the role of attractive forces in determining hydrodynamic properties, (2) to provide clearer evidence for the existence of a non-Markovian generalization of Newtons Law, (3) to examine the slip-stick boundary conditions in more detail by using a high spatial resolution of the streaming velocity profiles, (4) to investigate the significance of the recently proposed cross-coupling coefficient[12,13] on the temperature profiles.

We compare the properties of three different systems, A, B, and C. In system A, fluid–fluid, fluid–solid, and solid–solid intermolecular interactions are governed by the purely repulsive part of the Lennard-Jones, or Weeks–Chandler–Andersen (WCA) potential.[14] In system B, these same interactions are now governed by the full 12-6 Lennard-Jones potential, truncated at 2.5σ. In system C, solid–solid and fluid–fluid interactions are governed by a WCA potential, but interactions between a fluid atom and a wall atom are governed by the same Lennard-Jones 12-6 potential as used in system B. Table I summarizes these differences. To minimize the computational effort, we only conduct the system C simulations at $H=4.0\sigma$. The data for the WCA fluid at $H=5.1\sigma$ is old data reproduced from an earlier publication.[9] The remaining data are new.

II. NAVIER–STOKES HYDRODYNAMICS

A. Streaming velocity and boundary conditions

In classical hydrodynamics, the streaming or flow velocity at a point is obtained by solving the Navier–Stokes momentum flow equation. For planar Poiseuille flow at low

---

[a]Author to whom correspondence should be addressed. Current address: Department of Chemistry, Imperial College, London SW7 2AY, United Kingdom.

J. Chem. Phys., Vol. 112, No. 4, 22 January 2000

Poiseuille flow in slit pores   1985

TABLE I. Potentials employed in the three systems simulated.

System	Fluid–fluid interactions	Wall–fluid interactions	Wall–wall interactions
A	WCA	WCA	WCA
B	LJ	LJ	LJ
C	WCA	LJ	WCA

Reynolds number for a simple fluid confined between two infinite parallel walls, the steady state continuity equation (for flow in the x-direction) is

$$\frac{d\Pi_{xz}}{dz} = -\frac{dp}{dx}, \tag{1}$$

where p is the equilibrium hydrostatic pressure, Π_{xz} is the xz element of the viscous part of the pressure tensor ($\mathbf{\Pi} = \mathbf{P} - p\mathbf{1}$), and z is the direction normal to the walls. The Navier–Stokes equation for momentum flow is then obtained by substituting the linear constitutive relation appropriate for an isotropic fluid,

$$\Pi_{xz}(z) = -\eta \frac{du_x(z)}{dz}, \tag{2}$$

in Eq. (1). Here η is the shear viscosity coefficient and u_x is the x-component of the streaming velocity. From Eq. (1) and (2) we have

$$\eta \frac{d^2 u_x(z)}{dz^2} = \frac{dp}{dx}. \tag{3}$$

Solving Eq. (3) leads to the general solution,

$$u_x(z) = -\frac{1}{2\eta} \frac{dp}{dx} (a^2 - z^2), \tag{4}$$

where a is a constant determined by the boundary conditions (the second arbitrary constant vanishes by symmetry).

To fully specify the streaming velocity, the usual practice is to assume no-slip boundary conditions, i.e., the tangental component of the velocity vanishes at the boundary. With this assumption, the constant, a, appearing in Eq. (4) is equal to $H/2$. Computer simulation studies of LJ fluids flowing past walls with molecular structure revealed that the no-slip condition was essentially correct.[15,16] In some cases, it was found that the tangental component of the streaming velocity extrapolated to zero at a position a few molecular diameters inside or outside the fluid. Koplik and Banavar refer to this phenomenon as ''microscopic slip,'' though they note that it is macroscopically insignificant.[17]

B. Local vs nonlocal viscosity

In obtaining Eq. (4) it has been assumed that the shear viscosity has no dependence on z, either explicitly or implicitly through any positional dependence of the state variables, p and T. It is also assumed that the shear viscosity is independent of the magnitude of the driving force, namely, the pressure gradient. In the weak flow limit, the last of these assumptions will be valid but, for high degrees of confinement, the positional dependence of the state variables, and

the transport properties, are expected to become significant. We note that even in wide channels, the density and hence transport coefficients can depend on the local z position if the temperature varies strongly with position as a result of viscous heating effects. The effect of these variations can be incorporated in the Navier–Stokes formalism. The analysis of Todd and Evans[13] for example, leads to a viscosity which varies with the fourth power of z, to leading order. To account for density variations resulting from confinement, Bitsanis et al.[3] introduced a nonlocal viscosity which is not a point function of z, but, rather, a function of the local average density at z. The local average density at z is obtained by averaging the local density over a spherical volume centered on z, with a diameter equal to σ. They called their method the local average density model, or LADM. Application of LADM requires a knowledge of the shear viscosity of a homogeneous fluid as a function of density for a given temperature, and an appropriately course grained density profile. Using LADM, Bitsanis et al.[3] calculated velocity profiles for a number of flow situations corresponding to a fluid confined by smooth, structureless walls. For planar Poiseuille flow, they obtained velocity profiles which deviated from the classical quadratic behavior when the pore width was reduced to 8σ or less. Pozhar–Gubbins theory,[18,19] when used in conjuction with a local generalization of Eq. (2) for the case of Poiseuille flow of a WCA fluid in a narrow pore, also predicts nonquadratic velocity profiles, though the deviations are weak.[20] It was pointed out by the authors of this paper that for pores as narrow as 5 molecular diameters, a possible replacement for the linear constitutive relation defined in Eq. (2) is the nonlocal form,

$$\Pi_{xz}(x) = -\int_0^z \eta(z; z - z') \gamma(z') dz', \tag{5}$$

where $\gamma(z) = \partial u_x / \partial z$ is the local strain rate. It is important to note that Eq. (5) is still a linear relationship. Nonlinear corrections would involve the so-called Burnett coefficients. Equation (5) implies that the stress generated at position z is not simply proportional to the strain rate at that point, but rather depends on the entire strain rate field which exists throughout the fluid. For sufficiently wide pores, where density inhomogeneities are weak, the viscous kernal will be proportional to a Dirac delta function, the constant of proportionality being the Navier–Stokes shear viscosity.

Travis et al.[9] found that for a simple fluid confined in a slit-pore only five molecular diameters wide, the velocity profile contained points of inflexion which imply local strain rates of zero. Use of Eq. (2) would lead to the viscosity being undefined at such points and lends weight to the use of Eq. (5) instead of Eq. (2) as the more useful definition of viscosity. The data obtained by Travis et al.[9] was from a simulation at a single pore width using a model of the confined fluid in which no attractive forces were present.

C. Temperature, heat flux, and thermal conductivity

The equation of change for the specific internal energy of a single component fluid composed of structureless, nonreacting particles is

$$\rho \frac{dU}{dt} = -\nabla \cdot \mathbf{J}_Q - \mathbf{\Pi} : \nabla \mathbf{u} - p \nabla \cdot \mathbf{u}, \tag{6}$$

where U is the specific internal energy and $\mathbf{J}_Q$ is the heat flux vector. For planar Poiseuille flow at steady state, Eq. (6) becomes

$$\frac{dJ_{Qz}(y)}{dz} = -\Pi_{xz}(z)\gamma(z). \tag{7}$$

The classical Navier–Stokes equation for heat flow applicable to planar Poiseuille flow is obtained by substituting Fourier's Law,

$$J_{Qz}(z) = -\lambda \frac{dT(z)}{dz} \tag{8}$$

into Eq. (7), to give

$$\lambda \frac{d^2 T(z)}{dz^2} = \Pi_{xz}(z)\gamma(z), \tag{9}$$

where λ is the thermal conductivity (assumed to be independent of position) and $T(z)$ is the local temperature at position z. Integrating Eq. (9) leads to an expression for the temperature profile for planar Poiseuille flow,

$$T(z) = T_0 - T_4 z^4, \tag{10}$$

where T_0 is the temperature at the midchannel plane, $z=0$, and T_4 is a constant determined by the boundary conditions.

In very narrow channels, the assumption of constant thermal conductivity is expected to be invalid. In wide channels, viscous heating may induce local variations in the density, which in turn can produce spatial variations in temperature, and ultimately, in the thermal conductivity. Todd and Evans[13] have discussed the consequences of allowing for these wide channel heat-induced variations upon the Navier–Stokes equations. Their analysis leads to a thermal conductivity that varies as the fourth power in z to leading order. The temperature profile however, remains quartic.

Baranyai, Evans, and Daivis[12] found that heat flow in a spatially inhomogeneous fluid could take place even in the absence of a temperature gradient. Consequently, they postulated a corrected version of Eq. (8),

$$J_{Qz}(z) = -\lambda \frac{dT(z)}{dz} + \xi \frac{d\gamma^2(z)}{dz}, \tag{11}$$

which includes the possibility of heat flow arising from variations in the square of the local strain rate. In the above equation, ξ is the strain rate induced cross coupling coefficient. Substituting Eq. (11) into the Navier–Stokes heat flow Eq. (7) leads to a temperature profile of the form,

$$T(z) = T_0 + T_2 z^2 + T_4 z^4 \tag{12}$$

which includes some quadratic character. Todd and Evans[13] conducted Poiseuille flow simulations at a pore width of 69σ and found that their temperature profiles indeed contained a quadratic signature, in agreement with Eq. (12) and in support of the correctness of Eq. (11). The existence of ξ seems unquestionable, but whether it can explain the results of Todd and Evans[13] is less clear. The value of ξ they obtain (about 100 in Lennard-Jones reduced units), seems rather

large. The system they studied is well into the nonlinear regime since the local streaming velocity becomes supersonic towards the center of their channel. In this regime, one would not expect heat induced strain rate coupling to be the sole nonlinear contribution to the hydrodynamic picture, and other sources could lead to a quadratic term in the temperature profile.

Liem, Brown, and Clarke[5] also found deviations from the hydrodynamic temperature profile in their results, obtained from computer simulations of planar Couette flow. Since there can be no strain rate induced heat flows for idealized planar Couette flow, it seems likely that Liem et al.'s temperature profile differed from the hydrodynamic prediction because of viscous heating effects.

Mansour et al.[10] also found deviations between their measured temperature profiles and those predicted from hydrodynamic theory. Their measured profiles were obtained from planar Poiseuille flow simulations using hard spheres. Their temperature profiles exhibited some quadratic character. They ascribed this effect to the breakdown of the assumption of local thermodynamic equilibrium. By lowering the Knudsen number (either by increasing the density or increasing the pore width) they found that the hydrodynamic temperature profile was recovered. When the mean free path of the molecules is large compared to the pore width, local equilibrium is seldom restored in the vicinity of the walls.

Finally, there remains a question mark over the use of a temperature in Eq. (11) which is based on the ideal gas thermometer. Recently, Ayton, Jepps, and Evans[21] have indicated that a temperature based upon the thermodynamic definition, $(\partial U / \partial S)|_V$ (the partial derivative of the internal energy with respect to the entropy at constant volume), may be the appropriate temperature to use in Eq. (11). In the weak flow regime, the ideal gas, or kinetic temperature, should become equivalent to the thermodynamic temperature.

III. METHOD

A. Simulation details

The NEMD technique used to simulate planar Poiseuille flow has previously been described in detail,[7,9,22,23] and here we only briefly outline the way in which the simulations were carried out. In our simulations we apply a constant force in the x direction to each particle, which has the same effect as allowing gravity to initiate the flow of fluid down the channel. The geometry of the system is shown in Fig. 1. Both the fluid and the wall atoms interact via a cut and shifted Lennard-Jones interatomic potential function defined by

$$\phi(r) = \begin{cases} 4\epsilon\left[\left(\dfrac{\sigma}{r}\right)^{12} - \left(\dfrac{\sigma}{r}\right)^6\right] - \phi(r_c) & r \leq r_c \\ 0 & r > r_c \end{cases}, \tag{13}$$

where r is the scalar interatomic distance, r_c is the truncation distance, and $\phi(r_c)$ is the value of the potential energy at the point of truncation while σ and ϵ are the Lennard-Jones distance and energy parameters. In all our simulations the wall atoms and fluid atoms have the same Lennard-Jones parameters and the same mass.
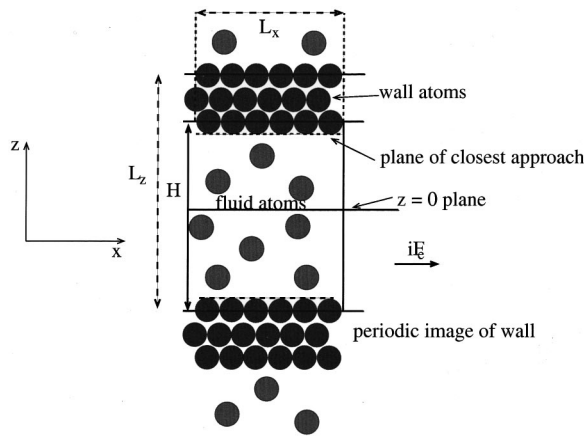
FIG. 1. Simulation geometry for planar Poiseuille flow. The y-axis is normal to the page.

Throughout the remainder of this paper we give all quantities in terms of Lennard-Jones reduced units (units defined in terms of σ, ϵ and the particle mass and will be denoted by the asterisk notation).

The WCA potential is a special case of the cut and shifted Lennard-Jones potential which is generated by truncating the potential at the distance for which it is a minimum, $2^{1/6}\sigma$. Because the WCA potential is shifted at the location of the energy minimum, it is a purely repulsive potential. We also consider a Lennard-Jones potential truncated and shifted at $r_c = 2.5\sigma$. This potential, which we henceforth refer to as the Lennard-Jones (LJ) potential, contains both an attractive and a repulsive contribution.

The system is surrounded by periodic images of itself in each of the three Cartesian dimensions. We note here that the simulation geometry is such that the applied force is in the x direction and the heat flow is in the z direction. We examine two different pore widths, $H = 5.1\sigma$ and $H = 4.0\sigma$. Here, H is defined as the separation in the z direction between the centers of the first layer of wall atoms adjacent to the fluid. For the $H = 5.1\sigma$ simulations we used a total of 360 fluid atoms bound by 216 wall atoms which were three atomic layers thick (72 atoms per layer). In the $H = 4.0\sigma$ simulations we used 288 fluid atoms but kept the number of wall atoms the same.

The wall atoms were fixed in a fcc lattice structure by harmonic restoring forces with a spring constant set to $150.15(\epsilon/\sigma^2)$, together with a holonomic constraint mechanism that fixed the center-of-mass of each layer of wall atoms, while allowing individual wall atoms the freedom to vibrate about their lattice sites. There is only one three-atom-thick wall per simulation cell. The second wall is simply the periodic image of the first wall. This periodicity also ensures that the total density of the system remains constant. Each layer of wall atoms has a surface density, $n_s^* = N_w \sigma^2/(L_x L_y) = 0.615$ (where N_w is the number of wall atoms per wall layer), while the layer separation is 1.085σ. For details of the governing equations of motion and the integrating scheme used to solve them, the reader is referred to Refs. 7, 22, 23.

The target density for all systems was $n^* = N\sigma^3/V$

$= 0.75$, where N is the number of fluid atoms and V is the volume accessible to the fluid. However the mean density calculated in the simulations was lower than this. We note that there is no unique average density of the fluid because there is no unambiguous definition for the volume accessible to the fluid. For the purpose of these simulations, we define the volume $V = L_x L_y l_z$, where l_z is $H - \sigma$ (see Fig. 1).

The walls of the system were maintained at a constant temperature of $T^* = Tk_B/\epsilon = 0.722$ and a number density of $n_w^* (\equiv 3N_w^*) = 0.85$. Temperature control was achieved by application of a Gaussian thermostat.[24] We stress here that the thermostat is applied to the wall atoms only. Viscous heat generated by the fluid is removed via conduction through the walls.

In all our simulations, we use a value of the applied force of 0.1 (ϵ/σ). This particular value was chosen in line with earlier work,[9] where 0.1 (ϵ/σ) was found to be large enough to promote measurable fluxes yet low enough to ensure that the system response remained linear. The simulations were started by equilibrating an initially crystalline fluid for two million time steps followed by a similar period of equilibration with the external field switched on. Production runs consisted of 1.6–2.4×10^7 time steps with a reduced time step $\tau^* = \tau(1/\sigma)\sqrt{\epsilon/m} = 0.001$.

B. Calculation of hydrodynamic quantities

To calculate the hydrodynamic properties of interest, we used the planes method of calculating the kinetic properties (PKP).[25,9] Briefly, one divides the simulation cell along the z direction into a number of equally spaced planes of area $L_x \times L_y$. The number density, kinetic energy density, and momentum density can then be evaluated at the planes positions by keeping track of the numbers of particles crossing each plane in a given direction with a given velocity and kinetic energy. The temperature and streaming velocity at the plane positions can then be evaluated using their hydrodynamic definitions. The expression for the momentum density at a plane is[25]

$$\bar{J}_x(z) = \lim_{\tau \to \infty} \frac{1}{\tau A} \sum_i \sum_{0 < t_{\alpha(i)} < \tau} \frac{m \dot{x}_i(t_{\alpha(i)})}{|\dot{z}_i(t_{\alpha(i)})|}, \tag{14}$$

where $\bar{J}_x(z)$ is the average momentum density at z, $\{t_{\alpha(i)}\}$ are the times α at which the z coordinate of particle i is equal to z, $\dot{x}_i$ and $\dot{z}_i$ are the x and z components of velocity of particle i, m its mass, τ is time interval over which we average the planes calculations and A is the xy-plane area. The mean number density at a plane, $\bar{n}(z)$, is given by a similar expression

$$\bar{n}(z) = \lim_{\tau \to \infty} \frac{1}{\tau A} \sum_i \sum_{0 < t_{\alpha(i)} < \tau} \frac{1}{|\dot{z}_i(t_{\alpha(i)})|}. \tag{15}$$

The average streaming velocity at a plane is defined through the hydrodynamic expression

$$\bar{J}_x(z) = m\bar{n}(z)\overline{u}_x(z), \tag{16}$$

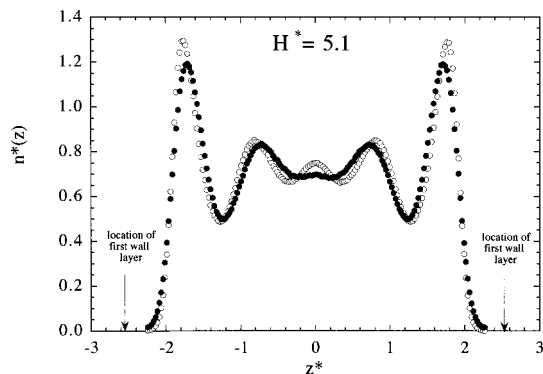while the local temperature is defined through

FIG. 2. Number density profiles for system A (WCA system, filled circles) and system B (LJ system, open circles) for $H^* = 5.1$ (error bars are too small to display).

$$\frac{1}{2m} \left\langle \sum_{i=1}^{N} [\mathbf{p}_i - m\mathbf{u}(z_i)] \cdot [\mathbf{p}_i - m\mathbf{u}(z_i)] \right\rangle$$

$$= \frac{(3\bar{n}(z) - \delta)}{2} \bar{T}(z)k_B, \tag{17}$$

where δ is the number of degrees of freedom used up in determining the local streaming velocity. The quantity on the left-hand side of Eq. (17) is the local peculiar kinetic energy at a plane. Note that the $\mathbf{p}$'s appearing in Eq. (17) are laboratory momenta.

In all our simulations we use a total of 200 planes to achieve a high resolution of properties.

IV. RESULTS AND DISCUSSION

A. Density profiles

The number density profiles obtained from the two pore widths are shown in Figs. 2 and 3. Taking first the 5.1 pore width (Fig. 2), we see that system B density profile shows five maxima, whereas system A profile shows four discernible peaks and one very weak peak in midchannel. The two peaks nearest the walls show that the fluid forms layers. The strength of the wall–fluid interaction determines the density of these layers. Attractive wall–fluid interactions result in more ordered layers (and hence higher density) near to the
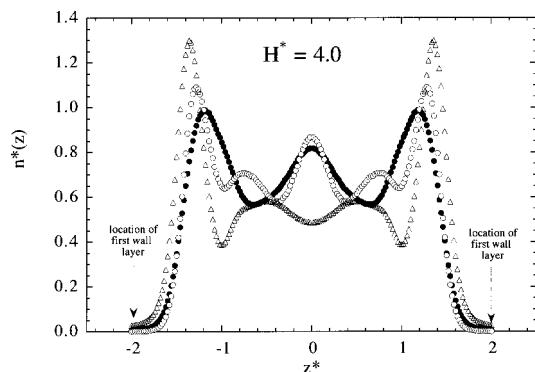

FIG. 3. Number density profiles for system A (WCA system, filled circles), system B (LJ system, open circles), and system C (fluid–fluid and solid–solid WCA, fluid–solid LJ, open triangles) for $H^* = 4.0$ (error bars are too small to display).
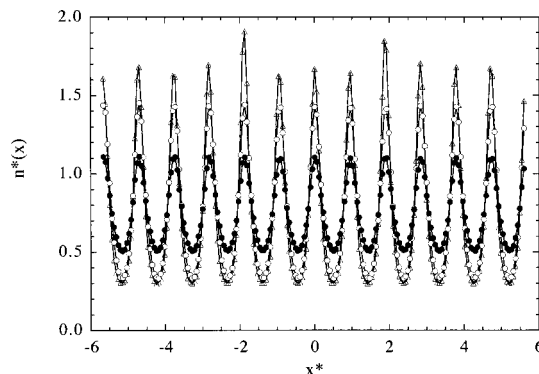

FIG. 4. Number density profiles as a function of x for $H^* = 4.0$: system A (WCA system, filled circles), system B (LJ system, open circles), and system C (fluid–fluid and solid–solid WCA, fluid–solid LJ, open triangles).

walls, as is evident in Fig. 2. The existence of high density fluid layers close to the walls induces the formation of fluid layers adjacent to these, which, in turn induce further layering, the effect becoming weaker with increasing distance from the walls. The induced layering effect is stronger in system B than in A, a fact attributed to the presence of attractive forces in the former. Since the fluid cannot support the existence of more than three layers in a slit pore of five molecular diameters, induced layering results in an oscillatory midchannel density profile, but these oscillations are relatively weak. We note that in both cases, the density falls to zero at $z^* = \pm 2.25$ while the walls are physically located at $z^* = \pm 2.55$ a fact which reflects the excluded volume arising from the finite size of the wall atoms.

The density profiles obtained from the $H^* = 4.0$ simulations are shown in Fig. 3. Once again, the system B profile has five maxima present but now, the midchannel peak has become more intense than the two surrounding peaks. The system A profile has only three maxima, corresponding to three fluid layers, while the system C profile possesses four maxima. A 20% decrease in slit-width has resulted in large differences between the fluid structure in the three systems, A, B, and C. Once more, we see that the presence of attractive wall–fluid forces leads to the formation of boundary liquid layers of higher density than is the case for repulsive wall–fluid interactions. The density of these layers is highest in system C, where the fluid atoms have a greater affinity for the wall atoms than they do for each other. The density profiles in both systems A and B fall to zero at the location of the walls, i.e., $z^* = \pm 2.0$. In the case of system C, the density profile does not go to zero at the location of the walls indicating that the fluid atoms are wetting the walls.

In Fig. 4 we show the density profiles in the direction of flow for the $H^* = 4.0$ simulations. In obtaining these profiles, we have averaged over the y and z variations. We see that the fluids are highly structured in all three systems. The density oscillates with a wavelength of the order of σ. Clearly the wall structure has been imposed upon the fluid. This lateral ordering effect has been seen previously in equilibrium simulations of confined fluids.[2] The amplitude of the density oscillations increases with the inclusion of attractive wall-fluid contributions and is largest for system C.

J. Chem. Phys., Vol. 112, No. 4, 22 January 2000

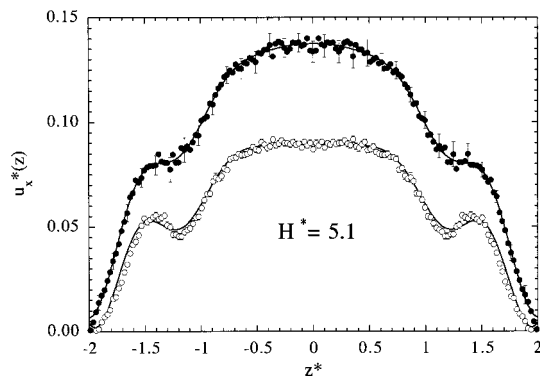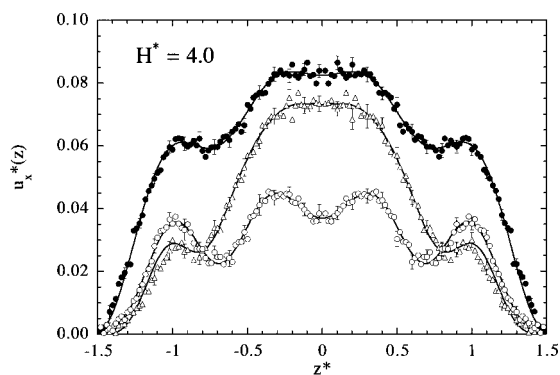Poiseuille flow in slit pores   1989

FIG. 5. Streaming velocity data for $H^* = 5.1$ together with curves obtained from fitting Eq. (18) to the velocity data. Only the data lying inside the no-slip planes is shown; system A (WCA system, filled circles) and system B (LJ system, open circles).

B. Flow velocity profiles

The streaming velocity profiles obtained from the $H^* = 5.1$ simulations are shown in Fig. 5. The profiles for both systems A and B are of similar shape. Neither profile is quadratic; however, they possess an underlying quadratic signature with superimposed oscillations. The two velocity profiles differ in magnitude, possibly a result of their difference in fluid temperature (see Figs. 13 and 14). The side lobes on the system B profile are also more pronounced than for system A, and the profile is flatter towards the center of the pore. The velocity, in both cases, extrapolates to zero at $z^* = \pm 2.0$ while the walls are located at $z^* = \pm 2.55$.

Figure 6 shows the streaming velocity profiles from the $H^* = 4.0$ simulations. All profiles deviate from the continuum quadratic form. In the system B case, there are four clear maxima present, while for systems A and C, only three are discernible. While all three velocity profiles extrapolate to zero at roughly the same point ($z^* = \pm 1.5$), the curvature of the profiles close to the point of zero velocity is different. The system A velocity profile is closest in form to that predicted by Bitsanis et al.[11] for the same pore width, although the side lobes on our simulated profile are much more pronounced than their theory predicts.

FIG. 6. Streaming velocity data for $H^* = 4.0$ together with curves obtained from fitting Eq. (18) to the velocity data. Only the data lying inside the no-slip planes is shown: system A (WCA system, filled circles), system B (LJ system, open circles), and system C (fluid–fluid and solid–solid WCA, fluid–solid LJ, open triangles).

The nonzero value of the velocity profiles at the wall locations has been interpreted by Koplik and Banavar[17] as microscopic slip. At the pore widths we have studied, the pore volume cannot be expressed without ambiguity. The excluded volume of implicit wall atoms becomes increasingly significant as the pore width decreases. If the pore width is defined by the plane of closest approach to the wall atoms then the velocity profiles appear to extrapolate to zero at *this* point (at least within the statistical uncertainties of our data). With this interpretation, our results could be taken to imply that slip does not occur. More precise data is needed to qualify this.

The location of the no-slip planes seems to be independent of the nature of the wall–fluid interaction and also independent of whether the wall–fluid and fluid–fluid interactions are the same. Furthermore, it appears to be independent of pore width, being located 0.5 molecular diameters away from the walls in all cases.

Following Travis et al.,[9] we have tried a functional fit to our streaming velocity data that retains the Navier–Stokes solution with the addition of a truncated Fourier cosine series, to account for the deviations from classical behavior. This latter contribution is justified on the grounds that for a fully periodic system, the local streaming velocity will be a periodic function of the z coordinate. Thus, the velocity is fitted to

$$u_x(z) = a_0 + a_1 z^2 + \sum_{n=2}^{n_{max}} a_n \cos\left[\frac{2\pi(n-1)z}{H^{*eff}}\right], \qquad (18)$$

where n is an integer, H^{*eff} is the effective pore width and the quantities $a_0 \ldots a_n$ are undetermined constants. We define the effective pore width to be twice the value of the no-slip plane location. For the two pore widths we studied, $H^* = 4.0$ and $H^* = 5.1$, H^{*eff} turns out to be 3 and 4, respectively. We find that 8 terms are needed to adequately represent the $H^* = 5.1$ data. For $H^* = 4.0$, 9 terms are required to fit the system C velocity profile, 8 terms are needed for the system B data, and only 6 terms are required to describe the system A profile. Figures 5–6 show the velocity data from $H^* = 4.0$ and 5.1 simulations together with the least squares fit curves obtained from fitting the data to Eq. (18). Equation (18) provides a reasonable fit to the profiles, but it tends to lead to incorrect behavior close to the no-slip plane.

C. Strain rate profiles

The scalar strain rate is defined as the nonvanishing component of the strain rate tensor $\nabla \mathbf{u}$, which, for planar Poiseuille flow is

$$\gamma(z) = \frac{du_x(z)}{dz}, \qquad (19)$$

from which it follows that the classical Navier–Stokes strain rate profile will be a linear function of the coordinate z, normal to the confining walls. Since our simulated streaming velocity data deviate from classical behavior, we do not obtain linear strain rate profiles. Based on the function used to fit our streaming velocity data, Eq. (18), we can calculate a nonclassical strain rate curve from
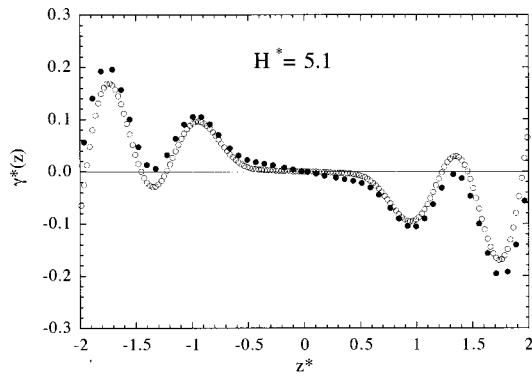
FIG. 7. Strain rate profiles for $H^* = 5.1$: system A (WCA system, filled circles) and system B (LJ system, open circles). These profiles were obtained from Eq. (20) using the least squares fit coefficients obtained from fitting the velocity profiles.

$$\gamma(z) = 2a_1 y - \frac{2\pi}{H^{*\mathrm{eff}}} \sum_{n=2}^{n_{\max}} a_n (n-1) \sin \left[\frac{2\pi(n-1)z}{H^{*\mathrm{eff}}} \right]. \quad (20)$$

This method is to be preferred over numerical differentiation of the streaming velocity data, since the latter method yields profiles which contain too much statistical noise.

The strain rate profiles obtained from Eq. (20) for the $H^* = 5.1$ simulations are shown in Fig. 7. We have truncated the strain rate fits at the location of the no-slip interface ($z^* = \pm 2.0$). From the figure we see that both the system A and system B strain rate profiles display significant oscillations about an underlying linear trend. While the underlying slopes of the two strain rate profiles are slightly different, they have the same qualitative features. The period and wavelength of the oscillations are approximately the same. The fact that the two profiles differ in slope is a direct consequence of the temperature difference between the WCA and LJ fluids; the higher temperature of the former gives rise to a steeper velocity profile and hence greater strain rate. For this particular pore width there is remarkably little difference in the two strain rate profiles.

The strain rate profiles obtained from Eq. (20) for the $H^* = 4.0$ simulations are shown in Fig. 8. As for the $H^* = 5.1$ case, all profiles have an underlying linear trend with
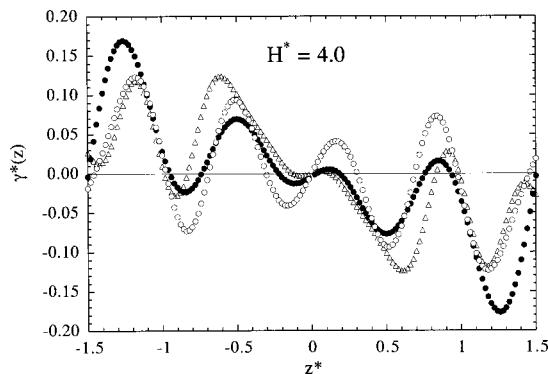

FIG. 8. Strain rate profiles for $H^* = 4.0$: system A (WCA system, filled circles), system B (LJ system, open circles), and system C (fluid–fluid and solid–solid WCA, fluid–solid LJ, open triangles). These profiles were obtained from Eq. (20) using the least squares fit coefficients obtained from fitting the velocity profiles.

superimposed oscillations. However, unlike the wider pore width example, the oscillations in these profiles are out of phase. This fact is a consequence of the number of terms used to fit the streaming velocity profiles for the three systems. The most important feature of Fig. 8 is the number of zeros present in the three profiles. In the case of the system A and B profiles, there are nine points at which the strain rate becomes zero, while for the system C profile, there are just seven such points. This difference however, is unlikely to be real; the system C profile has the wrong behavior in the vicinity of the no slip plane (it does not extrapolate to zero), which is an artifact stemming from the poor fit of Eq. (18) to the system C velocity profile close to the no-slip plane. The presence of zeros in the strain rate profiles implies that use of Eq. (2) would give rise to an unphysical shear viscosity containing singularities.

D. Stress profiles

The local stress, $\Pi_{xz}(z)$ may be calculated via two different methods; the so-called method of planes[7] or by direct integration of the hydrodynamic equation of motion. The former of these two methods yields an exact statistical mechanical expression for the pressure tensor evaluated at a plane. The second method is a mesoscopic method since it does not require any molecular information. Todd et al.[7] compared both of these methods in their simulations of a simple fluid undergoing planar Poiseuille flow and found that the mesoscopic method yielded superior statistics. We choose therefore, to use this latter method for calculating the stress in our simulations.

The mesoscopic expression for the stress $(-\Pi_{xz})$ follows from integrating

$$\frac{d\Pi_{xz}}{dz} = nF_e, \quad (21)$$

where F_e is the external force which drives the flow and n is the fluid number density. This equation is equivalent to Eq. (1) if an external force drives the flow rather than a pressure gradient, giving

$$\Pi_{xz}(z) = F_e \int_0^z n(z')dz' + C, \quad (22)$$

where C is a constant of integration whose value is determined by the fact that the stress is zero at the center of the channel.

One can also calculate the stress exerted by the fluid on the walls. From the definition of the pressure tensor, $\mathbf{P}$,

$$d\mathbf{F} = -\mathbf{P} \cdot d\mathbf{A} \quad (23)$$

we can write

$$-\Pi_{xz}^{\mathrm{walls}} = \frac{F_z^{\mathrm{walls}}}{L_x L_y}, \quad (24)$$

where F_z^{walls} is the total intermolecular force exerted on the layer of wall atoms in direct contact with the fluid by the fluid atoms. Equation (22) shows that the stress profile for planar Poiseuille flow will be a linear function of the z coor-
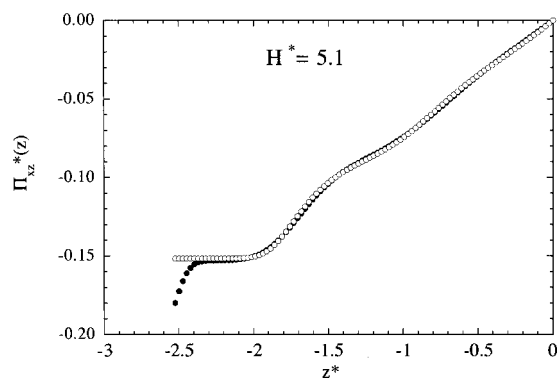
FIG. 9. Stress profiles for $H^*=5.1$: system A (WCA system, filled circles), and system B (LJ system, open circles). These profiles were obtained from numerically integrating the density profiles using the trapezoidal rule.

FIG. 11. Heat flux profiles for $H^*=5.1$: system A (WCA system, filled circles), system B (LJ system, open circles). These profiles were obtained from numerically integrating the product of the stress and strain rates using the trapezoidal rule.

dinate if the density is constant across the channel. In our simulations the density is nonuniform, yielding a nonlinear stress profile.

In Figs. 9 and 10 we show the stress profiles for the two pore widths, $H^*=5.1$ and $H^*=4.0$. These profiles were obtained through numerical integration (using the trapezium rule) of the density data. The profiles are displayed for only the left side of the channel. From Fig. 9 we see that both the system A and system B profiles deviate only a little from the classical linear form. The stress levels out at roughly the location of the no-slip plane ($z^*=-2$). There is good agreement between the two stress profiles across the entire range except for one or two points very close to the walls.

In Fig. 10 we see that the deviations in the three stress profiles from linearity are more significant than was the case for $H^*=5.1$. The oscillations are typically of longer wavelength. The stress profiles for system A and B are very similar, while the system C profile differs markedly across the entire range of z from these two. The different nature of the wall-fluid and fluid–fluid interactions in the system C case has a significant effect on the fluid stress. By contrast, a lack of attractive interactions in the system A fluid give rise to a weak effect on the fluid stress. As for the $H^*=5.1$ case, the stress profiles level out at approximately the location of the
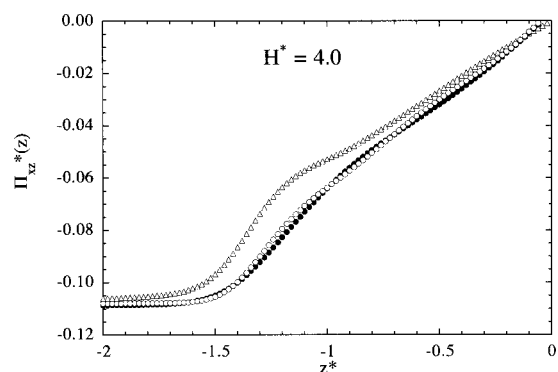
no-slip plane. The value of the stress at this point is equal to the stress at the walls calculated independently via Eq. (24).

E. Heat flux and temperature profiles

The heat flux across the channel may be calculated via a mesoscopic route similar to the method used for calculating the nonequilibrium stress, or via a method of planes (MoP) expression. The MoP route to the heat flux[22] utilizes an exact statistical mechanical expression for $\mathbf{J}_Q$. However, as Travis and co-workers point out,[9] the MoP expression for $\mathbf{J}_Q$ relies on an *a priori* knowledge of the instantaneous streaming velocity, which is not known accurately in the simulation. A poor guess for the streaming velocity can lead to an incorrect heat flux profile being measured. In this work we therefore choose a mesoscopic route to the heat flux. Integration of Eq. (7) yields

$$J_{Qz}(z) = -\int_0^z \Pi_{xz}(z')\,\gamma(z')\,dz' + C, \tag{25}$$

where C is an arbitrary constant determined from the fact that the heat flux is zero at $z^*=0$. Inspection of Eq. (25) reveals that the classical heat flux profile should be a cubic polynomial in z.

The heat flux profiles obtained from the $H^*=5.1$ simulations for system A and B are shown in Fig. 11. We see that both profiles clearly deviate from the classical solution. System A and B profiles have the same qualitative features but the latter heat flux extrapolates to a greater magnitude at the no-slip interface ($z^*=-2.0$).

The heat flux profiles obtained from the $H^*=4.0$ simulations for systems A, B, and C are shown in Fig. 12. All three profiles display significant deviations from the classical result. Qualitatively, all profiles show similar features but they differ in the amplitude and wavelength of the oscillation centered around $z^*=-1.0$. The magnitude of the system A heat flux is greater at the no-slip interface ($z^*=-1.5$) than either the system B or system C heat fluxes.

The temperature across the channel in each of our simulations is calculated from Eq. (17). In Fig. 13 is shown the temperature profiles obtained from the $H^*=5.1$ simulations together with the curves representing the least squares fit of

FIG. 10. Stress profiles for $H^*=4.0$: system A (WCA system, filled circles) system B (LJ system, open circles), and system C (fluid–fluid and solid–solid WCA, fluid–solid LJ, open triangles). These profiles were obtained from numerically integrating the density profiles using the trapezoidal rule.
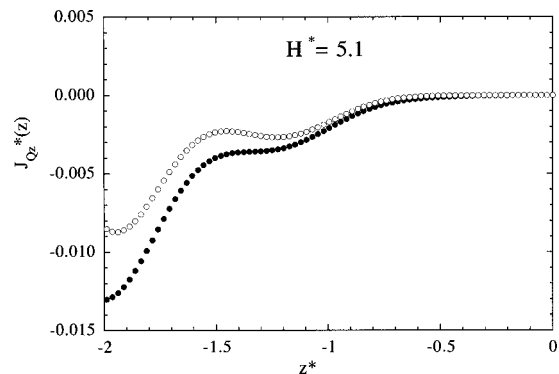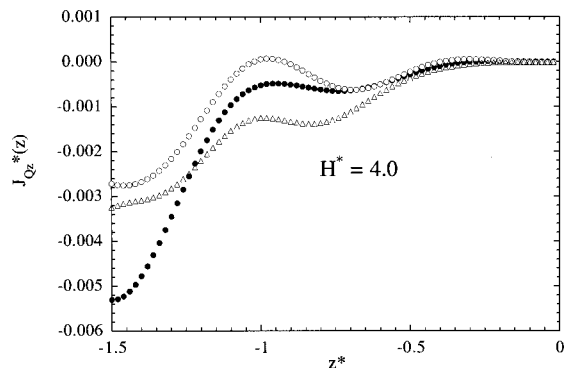
FIG. 12. Heat flux profiles for $H^* = 4.0$: system A (WCA system, filled circles), system B (LJ system, open circles), and system C (fluid–fluid and solid–solid WCA, fluid–solid LJ, open triangles). These profiles were obtained from numerically integrating the product of the stress and strain rates using the trapezoidal rule.

FIG. 14. Temperature profiles for $H^* = 4.0$: system A (WCA system, filled circles), system B (LJ system, open circles), and system C (fluid–fluid and solid–solid WCA, fluid–solid LJ, open triangles). The solid lines are the least squares fit curves of Eq. (10) to the temperature data. Symbols are displayed for every second data point to maintain clarity.

Eq. (10) to the data. Both profiles are almost linear and featureless. In the case of the system B results, the temperature rises slightly in the pore compared to the wall temperature ($T_0^* = 0.749$ while $T_w^* = 0.722$). The system A case is rather different. Here, $T_0^* = 0.951$, which implies a very large difference between the wall and fluid temperatures. Looking at Fig. 14, we see much the same situation at $H^* = 4.0$. There is only a small difference between the system B and system C temperature profiles but a very large difference between them and the system A profile.

Lack of attractive interactions between the wall and fluid atoms gives rise to a very poor thermal coupling between the wall and fluid momenta. The system A case is clearly unphysical in that very large temperature gradients are present in the region close to the walls. It is this higher temperature that is responsible for the higher flow velocity exhibited by system A. It should be noted that this large temperature jump is not unique to these simulations, and is therefore not a function of the high degree of confinement; similar temperature jumps can be seen in pores of width 69σ.[13]

Within the accuracy of our temperature data we find no evidence of a quadratic term, which might be expected on the basis of either strain rate coupling or from a possible breakdown of local thermodynamic equilibrium.
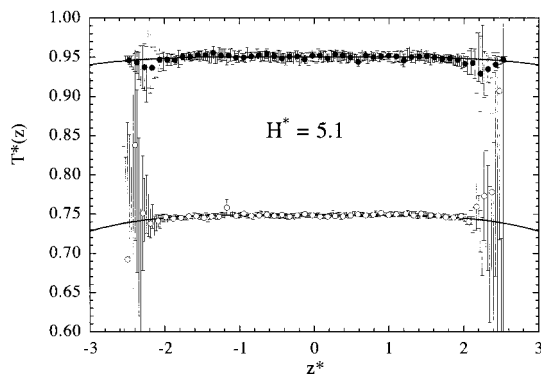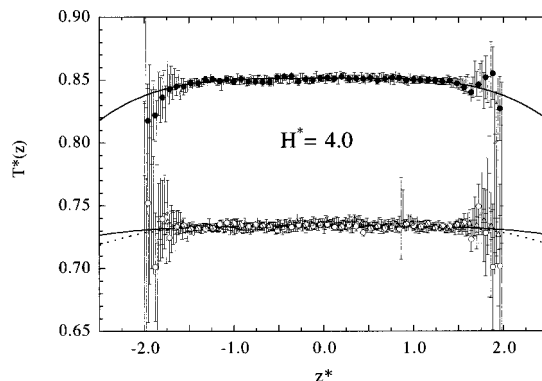
F. Viscosity and thermal conductivity

In Sec. IV C the point was made that the strain rate profiles contained zeros. By symmetry, the strain rate must be zero at the center of the channel and hence the Navier–Stokes shear viscosity is undefined at this point. However, the presence of zeros elsewhere in the strain rate profile implies that Eq. (2) is incorrect in general.

In Figs. 15 and 16 we show the local shear viscosity for the two different pore widths, $H^* = 5.1$ and $H^* = 4.0$. The shear viscosity in these plots was calculated using Eq. (2),

$$\eta(z) = \frac{-\Pi_{xz}(z)}{\gamma(z)}. \tag{26}$$

In all cases, the shear viscosity profile displays discontinuities resulting from zeros in the strain rate profiles. To procede any further with the analysis, one could take spatial Fourier transforms of the stress and strain rate profiles, then evaluate the wave vector dependent viscosity via

$$\tilde{\Pi}_{xz}(k_z) = -\tilde{\eta}(k_z)\tilde{\gamma}(k_z) \tag{27}$$

which follows from taking the 1D spatial Fourier transform of Eq. (5) (denoted by a tilde). An effective Navier–Stokes shear viscosity would then be obtained by taking the zero wave vector limit of $\tilde{\eta}(k_z)$. We tried such an analysis on our
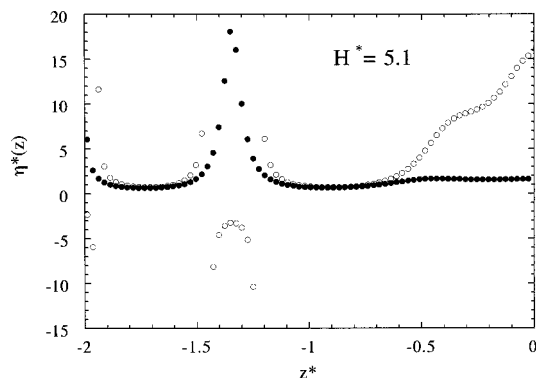

FIG. 13. Temperature profiles for $H^* = 5.1$: system A (WCA system, filled circles) and system B (LJ system, open circles). The solid lines are the least squares fit curves of Eq. (10) to the temperature data. Symbols are displayed for every second data point to maintain clarity.

FIG. 15. Shear viscosity for $H^* = 5.1$: system A (WCA system, filled circles) and system B (LJ system, open circles).
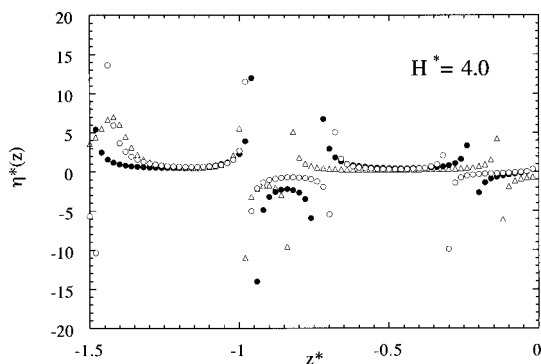
FIG. 16. Shear viscosity for $H^*=4.0$: system A (WCA system, filled circles), system B (LJ system, open circles), and system C (fluid–fluid and solid–solid WCA, fluid–solid LJ, open triangles).

FIG. 18. Thermal conductivity profiles for $H^*=4.0$: system A (WCA system, filled circles), system B (LJ system, open circles), and system C (fluid–fluid and solid–solid WCA, fluid–solid LJ, open triangles).

data but were unable to obtain meaningful and consistent wave vector dependent viscosities. We do not have a high enough spatial resolution in our profiles to enable accurate discrete Fourier transforms to be calculated.

Our results suggest that the simple linear constitutive relation Eq. (2) should be replaced by a more general relationship such as Eq. (5) in cases where the strain rate varies on a microscopic scale, such as is the case for highly confined fluids under flow.

We evaluate the thermal conductivities using Eq. (8) with the gradient in temperature obtained from differentiating Eq. (10). Figures 17 and 18 show the thermal conductivity profiles for $H^*=5.1$ and $H^*=4.0$, respectively. Only the data inside the no-slip planes is shown. In Fig. 17, the LJ thermal conductivity exhibits two oscillations; one centered at $z^*=-1.5$ and a larger amplitude oscillation centered at $z^*=-0.4$. The WCA thermal conductivity also displays oscillations, albeit weaker in amplitude, but in-phase with those of the LJ profile. In addition, the WCA thermal conductivity profile displays a peak around $z^*=-0.1$.

In Fig. 18, we show the thermal conductivity profiles for $H^*=4.0$. All three profiles exhibit oscillations in their thermal conductivity profiles. Once more, the oscillations are weakest in amplitude for the WCA case. All three profiles exhibit sharp increases at around $z^*=-0.25$. These sharp increases stem from the large uncertainty in calculating the
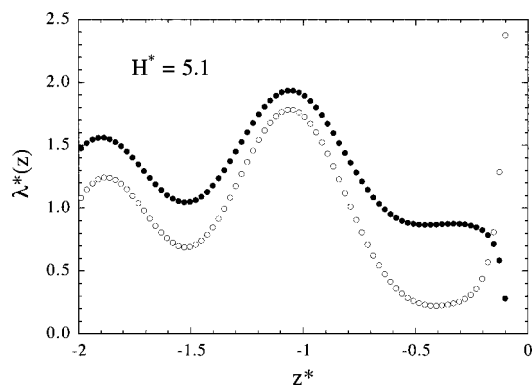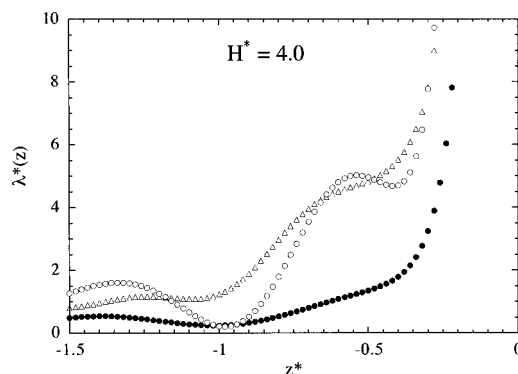
ratio of heat flux to temperature gradient near to the point where both quantities become close to zero.

Within the statistical uncertainties of our data there is little evidence to suggest that Fourier's Law, Eq. (8), must be replaced by a nonlocal generalization, analogous to the case of viscosity and Newton's Law.

V. SUMMARY

We have carried out NEMD simulations of simple fluids undergoing planar Poiseuille flow in a slit pore at two different pore widths, $H^*=5.1$ and $H^*=4.0$. Three different systems were studied. In one case, the WCA potential governs interactions between all pairs of atoms irrespective of whether they are wall atoms or fluid atoms. In another case, we used a Lennard-Jones potential, truncated and shifted at 2.5σ, to model interactions between all pairs of atoms. Finally, we considered the case where a WCA potential described interactions between pairs of wall atoms and between pairs of fluid atoms but with a Lennard-Jones potential to govern interactions between the wall and fluid atoms. These three fluid systems were studied so that we could examine the effects of attractive interactions on the hydrodynamic properties. In addition, we wanted to see how the simulated properties differed from continuum hydrodynamic predictions as the pore width became more narrow, such that excluded volume effects became significant.

At a pore width of five molecular diameters, the presence of attractive forces has a significant, but not large, effect on the density profile. The number of fluid layers formed is the same for the WCA and Lennard-Jones systems though the intensity of the midchannel density peak is greater in the latter system. It may seem surprising that the presence of attractive forces does not produce a more significant effect on the density profile close to the walls. However, the fluid–wall interactions are not very strong in our model. We stress that this wall model was used for convenience, and not as an attempt to closely model a particular real porous system.

When the pore width is lowered to four molecular diameters, more significant differences are seen between these two systems. The number of fluid layers formed is greater for the Lennard-Jones system than for the WCA system. This is a direct consequence of the greater excluded volume present

FIG. 17. Thermal conductivity profiles for $H^*=5.1$: system A (WCA system, filled circles) and system B (LJ system, open circles).

in the WCA system resulting from the absence of attractive forces. For system C, when the wall–fluid interactions are LJ but the fluid–fluid interactions are WCA, four fluid layers are present, but the two midchannel layers are quite diffuse. Again, this effect can be understood in terms of excluded volume and molecular packing effects.

We find that the streaming velocity profiles in all our simulations deviate from the continuum quadratic solution. Our results provide conclusive evidence that the Navier–Stokes equations break down for pore widths lower than five molecular diameters. This breakdown, being gradual (oscillations occur about an underlying continuum solution), suggests that it might be possible to extend hydrodynamics into the low wavelength regime. The origin of the departure from the classical Navier–Stokes profiles stems from the use of a local version of Newton's Law of viscosity, which is invalid if the fluid is highly inhomogeneous. The Navier–Stokes equation can be generalized by introducing a viscous memory kernal which accounts for nonhydrodynamic (i.e., low wavelength, high frequency) phenomena. We have suggested how one might test the validity of this generalization of Newtons Law, however, at present, we do not have sufficient spatial resolution in our stress and strain rate profiles to enable us to calculate the viscous memory kernal.

We have examined the behavior of the streaming velocity profiles in the region close to the walls in an attempt to establish the validity of the no-slip boundary conditions at microscopic distances. We find that velocity in all cases extrapolates to zero at a point inside the location of the walls. This phenomenon has in the past been interpreted as microscopic slip.[17] However, in narrow pores the excluded volume of the wall atoms becomes significant and one is no longer justified in defining the walls in terms of the center-of-mass of the innermost layer. Our results show that if one takes into account the excluded volume of the wall atoms, the no-slip boundary conditions are still obeyed in pore spaces of just a few molecular diameters. The curvature of the velocity profiles close to the no-slip interface is found to differ depending on the potential model chosen for the wall–fluid interaction; the presence of attractive forces results in the velocity profile becoming concave with respect to the ordinate.

Our calculated temperature profiles conform to the continuum predictions of a fourth order polynomial in the z-coordinate, at least within the present accuracy of our simulations. We do not find any evidence for a quadratic term, predicted from the modified form of Fourier's Law[12] and therefore conclude that the effects of any strain rate coupling are insignificant for pore spaces of these dimensions. The large temperature jump in the vicinity of the walls observed by Akhmatskaya et al.[20] and Todd and Evans,[13] is reproduced in our results, although only in cases where there is no attractive component to the wall–fluid interction energy. Lack of an attractive tail in this potential gives rise to poor thermal coupling between the fluid and the wall. The thermal conductivity was calculated using Fourier's Law and was found to exhibit oscillations across the pore. These oscillations originate from oscillations in the heat flux profile. We find no evidence for singularities in the thermal conductivity, unlike the case for shear viscosity.

In summary then, our results confirm the breakdown of Navier–Stokes equations for fluids contained within confined spaces of the order of five or fewer molecular diameters. The observed break down occurs in a gradual way and may provide the basis for an attempt to extend hydrodynamics to lower wave vector regimes.

[1] S. Toxvaerd, J. Chem. Phys. **74**, 1998 (1981).
[2] J. H. C. M. Schoen and D. J. Diestler, J. Chem. Phys. **87**, 5464 (1987).
[3] I. Bitsanis, J. J. Magda, M. Tirrell, and H. T. Davis, J. Chem. Phys. **87**, 1733 (1987).
[4] U. Heinbuch and J. Fischer, Phys. Rev. A **40**, 1144 (1989).
[5] S. Y. Liem, D. Brown, and J. H. R. Clarke, Phys. Rev. A **45**, 3706 (1992).
[6] P. Padilla and S. Toxvaerd, J. Chem. Phys. **101**, 1490 (1994).
[7] B. D. Todd, D. J. Evans, and P. J. Daivis, Phys. Rev. E **52**, 1627 (1995).
[8] W.-J. Ma, L. K. Iyer, S. Vishveshwara, J. Koplik, and J. Banavar, Phys. Rev. E **51**, 441 (1995).
[9] K. P. Travis, B. D. Todd, and D. J. Evans, Phys. Rev. E **55**, 4288 (1997).
[10] M. M. Mansour, F. Baras, and A. L. Garcia, Physica A **240**, 255 (1997).
[11] I. Bitsanis, T. K. Vanderlick, M. Tirrell, and H. T. Davis, J. Chem. Phys. **89**, 3152 (1988).
[12] A. Baranyai, D. J. Evans, and P. J. Daivis, Phys. Rev. A **46**, 7593 (1992).
[13] B. D. Todd and D. J. Evans, Phys. Rev. E **55**, 2800 (1997).
[14] J. D. Weeks, D. Chandler, and H. C. Andersen, J. Chem. Phys. **54**, 5237 (1971).
[15] J. Koplik, J. R. Banavar, and J. F. Willemsen, Phys. Rev. Lett. **60**, 1282 (1988).
[16] J. Koplik, J. R. Banavar, and J. F. Willemsen, Phys. Fluids A **1**, 781 (1989).
[17] J. Koplik and J. R. Banavar, Annu. Rev. Fluid Mech. **27**, 257 (1995).
[18] L. A. Pozhar and K. E. Gubbins, J. Chem. Phys. **94**, 1367 (1991).
[19] L. A. Pozhar and K. E. Gubbins, J. Chem. Phys. **99**, 8970 (1993).
[20] E. Akhmatskaya, B. D. Todd, P. J. Daivis, D. J. Evans, K. E. Gubbins, and L. A. Pozhar, J. Chem. Phys. **106**, 4684 (1997).
[21] G. Ayton, O. G. Jepps, and D. J. Evans, Mol. Phys. **96**, 915 (1999).
[22] B. D. Todd, P. J. Daivis, and D. J. Evans, Phys. Rev. E **51**, 4362 (1995).
[23] B. D. Todd and D. J. Evans, J. Chem. Phys. **103**, 9804 (1995).
[24] D. J. Evans and G. P. Morriss, *Statistical Mechanics of Nonequilibrium Liquids* (Academic, London, 1990).
[25] P. J. Daivis, K. P. Travis, and B. D. Todd, J. Chem. Phys. **104**, 9651 (1996).